State-Interaction Approach for Evaluating g-Tensors within EOM-CC and RAS-CI Frameworks: Theory and Benchmarks

Sven Kähler[a], Antonio Cebreiro-Gallardo[b], Pavel Pokhilko[a,c], David Casanova[b,d,*], Anna I. Krylov[a,**]

[a] Department of Chemistry, University of Southern California, Los Angeles, CA 90089, USA

[b] Donostia International Physics Center (DIPC), 20018 Donostia, Euskadi, Spain

[c] Current address: Department of Chemistry, University of Michigan, Ann Arbor, Michigan 48109, USA

[d] IKERBASQUE, Basque Foundation for Science, 48009 Bilbao, Euskadi, Spain

* david.casanova@dipc.org; ** krylov@usc.edu

Abstract

Among various techniques designed for studying open-shell species, electron paramagnetic resonance (EPR) spectroscopy plays an important role. The key quantity measured by EPR is the g-tensor describing the coupling between an external magnetic field and molecular electronic spin. One theoretical framework for quantum chemistry calculations of g-tensors is based on response theory, which involves substantial developments that are specific to underlying electronic structure models. A simplified and easier-to-implement approach is based on the state-interaction scheme in which perturbation is included by considering a small number of states. We describe and benchmark the state-interaction approach using equation-of-motion coupled-cluster and restricted-active-space configuration interaction wave functions. The analysis confirms that this approach can deliver accurate results and highlights caveats of applying it, such as a choice of the reference state, convergence with respect to the number of states used in calculations, etc. The analysis also contributes towards a better understanding of challenges in calculations of higher-order properties using approximate wave functions.

I. INTRODUCTION

Electron paramagnetic resonance (EPR) spectroscopy [1], which measures the interaction of the electronic wave function with an external magnetic field, enables studying open-shell paramagnetic systems[2] such as radicals and transition-metal complexes. It is used extensively to investigate the structure and reactivity of paramagnetic systems,[3] for example, metallo-proteins,[4] molecular magnets,[5, 6] spin qubits, and reaction intermediates.

Electronic structure calculations play an important role in these studies.[6, 7] In particular, ab initio calculations can validate the conclusions inferred from experimental data and can be used to refine underlying models. There are numerous flavors of EPR,[8, 9] but for the purpose of providing context for g-tensors calculations, we focus on the most common technique—continuous wave EPR or CW-EPR.[10] In CW-EPR a sample is irradiated with a radio wave of a fixed frequency and the intensity of the absorbed radiation is measured as a function of the strength (direction) of an external magnetic field. The magnetic field splits the energy levels of paramagnetic species by virtue of the Zeeman effect. The magnitude of the energy difference depends on the strength of the applied magnetic field and the angular momentum of the magnetic system. When this energy difference matches the energy of the incoming radio wave, photons are absorbed, inducing transitions between energy levels. These resonant field strengths appear as peaks in the EPR spectra.

The magnetic response of the system depends on energy levels of the unpaired electrons, in particular, energy splittings within a multiplet that arise due to relativistic effects.[11] For electrons confined to molecules, the most significant relativistic interaction is spin–orbit coupling (SOC). A comprehensive discussion of various terms contributing to SOC in molecules is provided by the work of Harriman [2] and a detailed benchmark study by Perera *et al.* [12] illustrates their significance for small molecules using coupled-cluster (CC) response theory calculations.[12] These system-dependent energy shifts modify the profile of EPR spectra and can be used as fingerprints of paramagnetic molecules, providing information about spin density distributions. In contrast to an isotropic response of the free electron to an external magnetic field, the response becomes orientation-dependent in molecules and solids.

Experimental measurements are interpreted by representing magnetic properties by model spin-Hamiltonians that describe the state of the sample by a set of model spin vectors,

representing the effective spin at each paramagnetic center.[11] In the simplest example of just a single unpaired electron modeled by the spin vector $\vec{S}$ in a magnetic field $\vec{B}$, the spin Hamiltonian H_S is:

$$H_S = \mu_B \vec{S} \mathbf{g} \vec{B} \tag{1}$$

where μ_B is the Bohr magneton and $\mathbf{g}$ (commonly referred to as the g-tensor) is a 3×3 matrix that parametrically describes the coupling between the model spin and the magnetic field vectors. For more complex cases, spin Hamiltonians are employed to describe EPR spectra for single electronic and multiple nuclear spins include parameterized spin–spin and spin–field interactions,

$$H_S = \mu_B \vec{S} \mathbf{g} \vec{B} + \vec{S} \mathbf{D} \vec{S} + \sum_A \left[\mu_N \vec{I}_A \mathbf{g}_N^{(A)} \vec{B} + \vec{I}_A \mathbf{D}^{(A)} \vec{I}_A + \vec{S} \mathbf{A}^{(A)} \vec{I}_A \right] + \sum_{A<B} \vec{I}_A \mathbf{J}^{(AB)} \vec{I}_B \tag{2}$$

where μ_N is the nuclear Bohr magneton, $\vec{S}$ the electronic spin, and $\vec{I}_A$ the nuclear spin of atom A. The 3×3 matrices $\mathbf{D}$ and $\mathbf{D}^{(A)}$ respectively describe the electronic and nuclear zero-field splittings, i.e., energy gaps between different spin projections in the absence of an external magnetic field. The $\mathbf{g}$ ($\mathbf{g}_n^{(A)}$) matrix parameterizes the coupling between the electronic (nuclear) spin and the magnetic field. $\mathbf{A}^{(A)}$ is the hyperfine coupling tensor that describes the interaction between nuclear and electronic spins, and $\mathbf{J}^{(AB)}$ parameterizes the interaction between nuclear spins. In the present work, we focus on the calculation of the components of the electronic matrix $\mathbf{g}$ only. Following the common convention, we report shifts in g-tensor values (Δg) relative to the electron spin g-factor, g_e=2.002319, so that

$$\mathbf{g} = g_e \mathbf{I} + \Delta \mathbf{g}. \tag{3}$$

Numerous electronic structure methods have been used to evaluate the components of $\mathbf{g}$ in paramagnetic molecules. These approaches broadly fall into two groups—they use either response theory[13, 14] or a state-interaction ansatz.[15] In the response theory approach the parameters of the underlying model wave function are adjusted to the perturbing magnetic field. Therefore, each electronic structure model requires a separate implementation to compute the perturbed electronic wave function. A response theory approach has been implemented for many models: unrestricted [16] and restricted open-shell Hartree–Fock (UHF

and ROHF, respectively),[17–19] density functional theory (DFT),[3, 20–22] multiconfigurational self-consistent field (MCSCF),[23] coupled-cluster with single and double (CCSD) and higher substitutions (CCSDT and CCSDTQ),[24] and multireference configuration interaction (MRCI).[25] However, it is not yet available for many other correlated methods, such as equations-of-motion coupled-cluster (EOM-CC),[26–28] algebraic diagrammatic construction (ADC),[29, 30] and restricted-active-space configuration interaction (RAS-CI).[31, 32] Consequently, reliable computational treatment of systems with more complex electronic structures remains challenging. Open-shell systems,[33] in particular, transition-metal compounds, pose challenges to electronic structure theory for which there is not yet a universally applicable solution.[33, 34]

In state-interaction approaches, the magnetic field and relativistic effects (i.e., SOC) are treated as couplings between eigenstates of the field-free non-relativistic Hamiltonian. The eigenstates of the spin–orbit coupled Hamiltonian (i.e., the Kramers pair in spin-doublet systems), are expressed as a linear combination of a limited number of uncoupled eigenstates of the spin-free Hamiltonian. The truncation of the set of interacting states to a small number of states can be justified by perturbation theory arguments. The attractive feature of the state-interaction approach is that it does not require derivation and implementation of magnetic-field-perturbed equations and, therefore, is much easier to apply—only electronic energies and matrix elements of the SOC and angular momentum operators are required. Furthermore, the state-interaction approach does not assume a vanishing perturbation, so if all states are included in the calculation, it yields the exact result for the relativistic states, whereas response theory yields the result corresponding to the non-relativistic states under a weak perturbation. In other words, the limits of state interaction and response theory are different, because the state interaction yields g-tensor for an all-orders relativistic Kramers doublet, whereas response theory yields g-tensor only for the first-order relativistic doublet. The drawback of the state-interaction approach is that the convergence with respect to the number of states included in the calculation is not known *a priori*. Despite these limitations, the state-interaction approach is extensively used[35] for including relativistic effects in quantum-chemistry calculations, for example, for evaluating spin–orbit interactions.[11, 36–50]

Several effects contribute to the g-tensor shift and their relative magnitudes are system-dependent. For molecules composed of light elements and first-row transition-metal com-

plexes, we use the perturbative approach introduced by Abragam and Bleaney.[51] In these systems, the main contribution results from a combined effect of paramagnetic SOC and orbital angular momentum, with smaller contributions from diamagnetic SOC and relativistic mass correction. Following other works that use state-interaction approaches,[39, 44] we limit ourselves to the paramagnetic spin–orbit coupling orbital and angular momentum terms.

In the state-interaction approach, the g-tensor is expressed in terms of matrix elements of spin and angular momentum between spin–orbit coupled states Φ_I, which goes back to an expression introduced by Gerloch and McMeeking.[15] The starting point for this approach is the non-relativistic Hamiltonian (H_0) perturbed by the spin–orbit part of the Breit–Pauli Hamiltonian and an external magnetic field (Zeeman term)

$$H = H_0 + H^{SOC} + \mu_B(\mathbf{L} + g_e\mathbf{S})\mathbf{B}. \tag{4}$$

The SOC term, H^{SOC}, is computed as matrix elements of the spin–orbit part of the Breit–Pauli Hamiltonian[36–38, 43, 45, 47–49]

$$H^{SOC}_{IJ} = \langle I|\, H^{SOC}\, |J\rangle\,, \tag{5}$$

where I and J denote non-relativistic states. To describe the two-electron part of the paramagnetic SOC, we use an effective one-electron spin–orbit mean-field treatment[43] using recently reported implementations.[45, 47, 48] Spin–orbit perturbed states are then obtained by diagonalizing the (SOC) perturbed Hamiltonian matrix

$$H^{eff}_{IJ} = E_I\delta_{IJ} + H^{SOC}_{IJ}, \tag{6}$$

constructed using a small number of non-relativistic electronic states with energies $\{E_I\}$, as justified by quasi-degenerate perturbation theory. The resulting eigenstates can be used to compute spin–orbit-perturbed properties, such as matrix elements of dipole moment, spin, angular momentum operators, or even Dyson orbitals.[46]

Following this strategy, one arrives to the master-matrix approach[39] for computing

g-tensors. The master-matrix $\mathbf{G}$ is computed using the following expression:

$$\mathbf{G}_{kl} \equiv (\mathbf{g}\mathbf{g}^{\top})_{kl} = 2 \sum_{u,v=\Phi,\Phi'} \langle u|\hat{L}_k + g_e\hat{S}_k|v\rangle\langle v|\hat{L}_l + g_e\hat{S}_l|u\rangle. \tag{7}$$

Here indices l, k denote the Cartesian components of the spin and angular momentum operators, and Φ and Φ' are the two Kramers' components of the state of interest. In the matrix form

$$\mathbf{G}_{kl} = \sum_{m=x,y,z} (g_e\mathbf{\Sigma}_{km} + \mathbf{\Lambda}_{km})(g_e\mathbf{\Sigma}_{lm} + \mathbf{\Lambda}_{lm}), \tag{8}$$

where matrices $\mathbf{\Sigma}$ and $\mathbf{\Lambda}$ are obtained by transforming electronic spin S and angular momentum L into the basis of the spin–orbit-coupled eigenstates of Eq. (6).

The computed $\mathbf{G}$ matrix is then diagonalized:

$$\mathbf{G}\mathbf{C} = \mathbf{C}g^d \tag{9}$$

and the actual g-tensor matrix is assembled as:

$$\mathbf{g} = \mathbf{C}\sqrt{g^d}\mathbf{C}^{\dagger}. \tag{10}$$

This procedure is visualized in Fig. 1 and implemented in a post-processing *Python* script, which is now included in the *ezMagnet* suite[52] (see the Supporting Information (SI) for details).

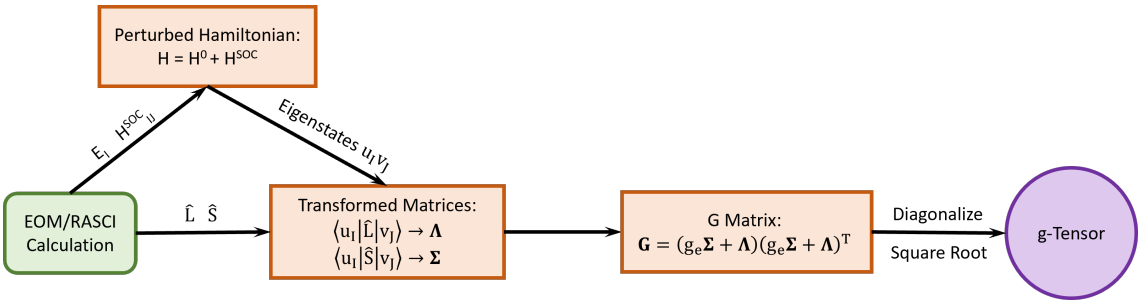

FIG. 1: Flowchart of state-interaction approach for calculations of g-tensors.

This approach, originally described[15] by Gerloch and McMeeking in 1975, simply follows from the mapping between the eigenstates of microscopic Hamiltonian, Eq. (4), and the phenomenological spin Hamiltonian, Eq. (1).

A useful approximate expression for the g-tensor shift, $\Delta\mathbf{g}_{TJ}^{\text{pert}}$, for doublet states is obtained by considering terms linear with the spin–orbit interaction, as was done in the Λ-tensor formalism introduced by Abragam and Bleaney[51]

$$\Delta\mathbf{g}_{0J}^{\text{pert}} = -4\mathbf{L}_{0J}\frac{H_{0J}^{SOC}}{\Delta E_{0J}}, \tag{11}$$

where $\mathbf{L}_{0J}$ are the transition angular moment matrix element, H_{0J}^{SOC} is the spin–orbit coupling matrix element, and ΔE_{0J} the energy difference between the ground state and the excited states, respectively.

In this work, we investigate the performance of the state-interaction approach using EOM-CC and RAS-CI wave functions obtained in single-reference calculations. We compare the results with previously published data as well as response-theory calculations using the unrestricted CCSD ansatz. We hope that these tools will extend the scope of open-shell systems amenable to high-level treatments.

The structure of the paper is as follows: in Section II we provide a brief overview of theoretical approaches used (EOM-CC[26] and RAS-CI) and essential computational details. In Section III we present the results for light molecules and transition-metal complexes and discuss the performance of various theoretical approaches. In addition to the effects of different correlation treatments, we also discuss computed electron distributions and solvent effects. Our concluding remarks are given in Section IV.

II. THEORETICAL AND COMPUTATIONAL DETAILS

Fig. 2 illustrates the essence of EOM and RAS-CI approaches to tackling open-shell species.[26, 53] Different types of target states can be accessed by a judicious choice of the reference and the excitation operator. Importantly, this approach can describe multi-configurational wave functions using a single-reference formalism (the term 'single-reference' refers to technical aspects of how the wave function is generated, i.e., from a single reference determinant, whereas 'multi-configurational' refers to the character of wave functions that comprise more than one configuration with a large coefficient). When used with closed-shell references, target open-shell wave functions are naturally spin-adapted. In both theories, the choice of the reference can affect the quality of the target states. The difference between

the two approaches is in how the excitation operators are parameterized.

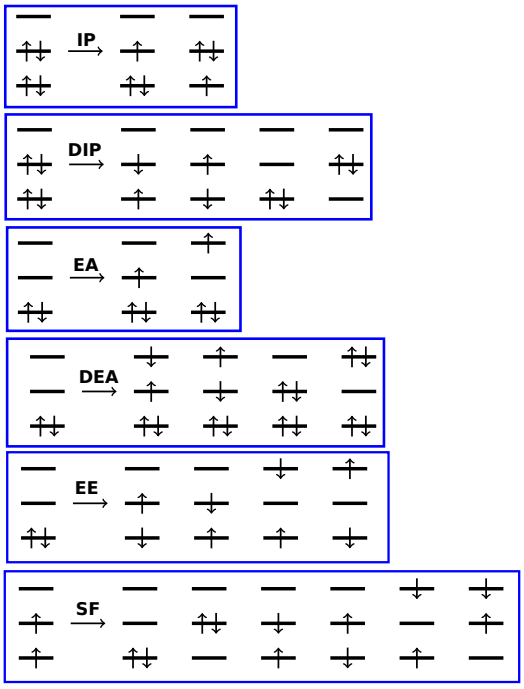

FIG. 2: In EOM-CC and RAS-CI methods, different types of target states can be accessed by different combination of the reference state and excitation operators. For example, doublet electronic states with one unpaired electron can be described by using ionizing or electron attaching operators acting on a closed-shell reference. Likewise, states with two unpaired electrons (diradicals) can be described using doubly ionizing, doubly electron attaching, or spin-flipping operators. Acronyms defining types of EOM operators: EE (excitation energies), IP (ionization potential), DIP (double IP), EA (electron attachment), DEA (double electron attachment), SF (spin-flip). *Reproduced from Ref. [53] with permission from the Royal Society of Chemistry.*

A. Equation-of-Motion Coupled-Cluster Approach for Open-Shell Systems

EOM methods are capable of describing electronic states with unpaired electrons because they can start from a closed-shell reference state for which reliable wave functions of suitable quality can be obtained with relative ease.[26–28] From a chosen reference, a subspace of electronic configurations for the target states, the Fock space, is then generated. Of particular interest here are the EOM methods that either add or remove an electron, i.e., EOM-IP and EOM-EA methods[26, 28, 54] (see Fig. 2). The reference wave function can be either a CCSD or an MP2 state. Using the respective amplitudes, a similarity transformed

Hamiltonian $\bar{H}$ can be constructed

$$\bar{H} = e^{-T} H e^{T} \tag{12}$$

where T is the excitation operator, which in the case of CCSD is given by the sum of single and double excitation operators:

$$T = \sum_{ai} t_i^a a_a^\dagger a_i + \frac{1}{4} \sum_{abij} t_{ij}^{ab} a_a^\dagger a_i a_b^\dagger a_j \tag{13}$$

with t_i^a and t_{ij}^{ab} as single and double amplitudes and $a_a^\dagger$ and a_i as creation and annihilation operators, respectively. Throughout this work, we follow the convention that the indices i and j denote occupied orbitals whereas a and b denote unoccupied orbitals in the reference determinant Φ_0. In EOM-CCSD, T amplitudes are found by solving the CCSD equations for the reference state, and in EOM-MP2, T_2 amplitudes are MP2 amplitudes. To obtain open-shell target states from closed-shell references a set of determinants with the correct number of electrons is generated. This is achieved by either adding or removing an electron, depending which option describes the target states better. The respective EOM amplitudes are found by diagonalizing the effective Hamiltonian $\bar{H}$. Because $\bar{H}$ is non-Hermitian, both the left and right sets of eigenstates need to be computed:

$$\bar{H}\mathcal{R} \left|0\right\rangle = E\mathcal{R} \left|0\right\rangle \tag{14}$$

$$\mathcal{L}\bar{H} \left|0\right\rangle = E\mathcal{L} \left|0\right\rangle \tag{15}$$

The EOM-IP-CCSD operators $\mathcal{R}^{\mathtt{IP}}$ and $\mathcal{L}^{\mathtt{IP}}$ have the following form:

$$\mathcal{R}^{\mathtt{IP}} = \sum_{i} r_i a_i + \frac{1}{2} \sum_{ija} r_{ij}^a a_a^\dagger a_i a_j \tag{16}$$

$$\mathcal{L}^{\mathtt{IP}} = \sum_{i} l_i a_i^\dagger + \frac{1}{2} \sum_{ija} l_{ij}^a a_a a_i^\dagger a_j^\dagger \tag{17}$$

The EOM-EA-CCSD operators $\mathcal{R}^{\mathrm{EA}}$ and $\mathcal{L}^{\mathrm{EA}}$ are

$$\mathcal{R}^{\mathtt{EA}} = \sum_a r^a a_a^\dagger + \frac{1}{2}\sum_{iab} r_i^{ab} a_a^\dagger a_b^\dagger a_i \tag{18}$$

$$\mathcal{L}^{\mathtt{EA}} = \sum_a l^a a_a + \frac{1}{2}\sum_{iab} l_i^{ab} a_a a_b a_i^\dagger \tag{19}$$

The advantage of EOM-CC treatment is that it includes both dynamic and non-dynamic correlation and that multiple states can be computed in a single step, which results in their balanced treatment and simplifies the calculations of transition properties (here, spin–orbit couplings and matrix elements of the angular momentum operator). The disadvantage is that each EOM method can only describe a particular set of target states. As we illustrate below, this sometimes presents a problem. Additional details for the EOM protocol for g-tensor calculations are given in the SI.

B. Coupled-Cluster Response Theory

In response theory properties are defined as derivatives of the energy.[14] In this formalism, the g-tensor is given as

$$\mathbf{g} = \frac{1}{\mu_B}\left(\frac{\partial^2 E}{\partial\epsilon_B \partial\epsilon_S}\right)_{B,S=0} \tag{20}$$

where ϵ_B and ϵ_S are magnetic field and SOC strengths, respectively. By applying the well-established procedures of CC response theory,[24] we obtain the g-tensor by solving the amplitude response equations

$$-\langle\Phi_\mu|\,\bar{L}_y\,|\Phi_0\rangle + \sum_\nu \langle\Phi_\mu|\,\left[\bar{H},\tau_\nu\right]|\Phi_0\rangle\left(\frac{\partial T}{\partial\epsilon_y}\right)_\nu = 0 \tag{21}$$

and the response Lagrange multiplier equations

$$\begin{aligned}-\sum_\mu \langle\Phi_0|\,\frac{\partial\Lambda}{\partial\epsilon_y}\,|\Phi_\mu\rangle\,\langle\Phi_\mu|\,\bar{H}-E_0\,|\Phi_\nu\rangle = &-\langle\Phi_0(1+\Lambda)|\,[\bar{\mu}_y,\tau_\nu]\,|\Phi_0\rangle \\ &+\sum_\rho \langle\Phi_0(1+\Lambda)|\,\left[\left[\bar{H},\tau_\rho\right],\tau_\nu\right]|\Phi_0\rangle\left(\frac{\partial T}{\partial\epsilon_y}\right)_\rho,\end{aligned} \tag{22}$$

where τ denotes excitation operators with the indices μ, ν, and ρ running over all single and double excitations, and Λ is the Lagrange multiplier vector. For the exact expressions for the CC g-tensor we refer to the work of Gauss, Kállay, and Neese.[24] From the perturbed amplitudes and Lagrange multipliers, the perturbed density is obtained as

$$D^L_{pq} = \frac{\partial D_{pq}}{\partial \epsilon_L} = \langle 0| \Lambda^L e^{-T} \left\{ a^\dagger_p, a_q \right\} e^T |0\rangle + \langle 0| (1+\Lambda) \left[e^{-T} \left\{ a^\dagger_p, a_q \right\} e^T, T^L \right] |0\rangle , \tag{23}$$

with D denoting electron density and the braces $\{\}$ denoting commutators. The g-tensor is obtained by contracting the perturbed density with respect to the angular momentum with the spin–orbit integrals

$$\mathbf{g} = \sum_{pq} D^L_{pq} H^{SOC}_{pq}, \tag{24}$$

where H^{SOC} is the mean-field spin–orbit coupling term of the Hamiltonian. Following the work of Gauss, Kállay, and Neese, [24] we implemented the response-theory calculations for spin-unrestricted CCSD in the Q-Chem electronic structure package.[55, 56]

C. Restricted Active Space Configuration Interaction

The RAS-CI method is an attractive alternative to the approaches based on multi-reference functions such as complete-active-space (CAS) methods. RAS-CI is a single-reference approach in which the orbital space is split into three subspaces: RAS1 (doubly occupied orbitals), RAS2 (the active space, including fully correlated orbitals), and RAS3 (virtual orbitals), as shown in Fig. 3. Excitations that generate electron vacancies in RAS1 are called holes (h) and excitations that generate electrons in RAS3 are called particles (p).

As in EOM-CC and other single-reference methods, the performance of RAS-CI depends on the choice of the reference wave function Φ_0 (usually, the Hartree–Fock determinant) and an excitation operator $\hat{R}$ that generates the target states Ψ_I. Because RAS-CI is a configuration interaction method, the target states are expressed as linear combinations of Slater determinants and amplitudes are obtained by an iterative diagonalization of the

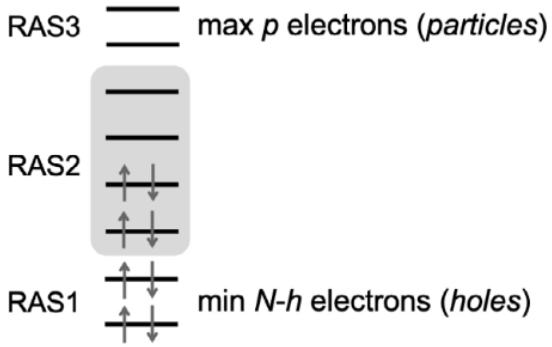

FIG. 3: Representation of RAS1, RAS2, and RAS3 subspaces in RAS orbital space [53].

Hamiltonian $\hat{H}$.

$$|\Psi_I\rangle = \hat{R}\,|\Phi_0\rangle = \sum_i c_i\,|\Phi_i\rangle \tag{25}$$

$$\sum_j \left\langle \Phi_i|\hat{H}|\Phi_j \right\rangle c_j = E c_i \tag{26}$$

Here, we use RAS-CI within the hole and particle (h,p) approach, RAS-CI(h,p), in which the excitation operator $\hat{R}$ is expanded in terms of single holes and particles. The hole/particle truncation of the excitation operator is attractive because of its low computational cost and can be expressed as:

$$\hat{R} = \hat{R}_0 + \hat{R}_h + \hat{R}_p \tag{27}$$

with

$$\hat{R}_0 = \sum_{\{s\}} r^{\{s\}} \left(\prod_{s\in \mathrm{RAS2}}^{n_0} a_s^\dagger \right) \left(\prod_{p\in|0\rangle}^{n_0} a_p \right), \tag{28}$$

$$\hat{R}_h = \sum_{\{s\},i} r_i^{\{s\}} \left(\prod_{s\in \mathrm{RAS2}}^{n_0+1} a_s^\dagger \right) a_i \left(\prod_{p\in|0\rangle}^{n_0} a_p \right), \tag{29}$$

$$\hat{R}_p = \sum_{\{s\},a} r^{a\{s\}} a_a^\dagger \left(\prod_{s\in \mathrm{RAS2}}^{n_0-1} a_s^\dagger \right) \left(\prod_{p\in|0\rangle}^{n_0} a_p \right), \tag{30}$$

where $\{r\}$ are the CI amplitudes, i, s and a run over all possible orbitals in RAS1, RAS2, and RAS3, respectively, index p is restricted to the n_0 RAS2 occupied orbitals in the reference configuration, and $\{s\}$ indicates a string of RAS2 spin-orbitals. Note that $\hat{R}_0$ contains

all possible configurations within RAS2, i.e., it is a CAS, whereas $\hat{R}_h$ and $\hat{R}_p$ generate all electronic configurations with one hole in RAS1 and one electron in RAS3, respectively. Typically, RAS1 (RAS3) contains the entire set of orbitals below (above) the RAS2 set.

In this work, we use four different excitation operators within the RAS-CI(h,p) framework: particle- and spin-conserving excitations (EE), spin-flip (SF) operators that generate states with different M_S with respect to the reference configuration Φ_0, electron attaching (EA) and ionizing (IP) operators that add or remove electrons, respectively (see Fig. 2). One of the main advantages of the RAS-CI(h,p) approach relative to other multiconfigurational methods is that the presence of configurations beyond the fully correlated orbital space can be used as a guide to expand and improve the RAS2 space by including relevant RAS1/RAS3 orbitals. Details on the selection of the RAS2 space, reference configuration, and excitation operator for each studied system are given in the SI. All RAS-CI calculations of electronic state energies and interstate couplings have been performed with the Q-Chem package.[55]

III. RESULTS AND DISCUSSION

To benchmark the state-interaction protocol using EOM-CC and RAS-CI wave functions, we use three small molecules from Bolvin's study [39] (H_2O^+, NO_2, CO_2^-) and eight first-row transition metal complexes shown in Fig. 4. The geometries of H_2O^+, NO_2, CO_2^- were taken from Ref. 39 and the geometries of transition-metal complexes were taken from Singh *et al.*[44] All Cartesian geometries are given in the SI. Symmetry labels and molecular orientations follow Mulliken's convention,[57] which is different from Q-Chem's standard orientation.[58] All calculations were carried out with the def2-TZVP basis set unless indicated otherwise.

As discussed above, the quality of the results depends critically on the choice of the reference and the excitation operator for both EOM-CC and RAS-CI methods. In RAS-CI, the exact partitioning of the orbital spaces is also critical. An important difference between the two methods is that EOM-CC includes dynamic correlation through the similarity transformation, whereas RAS-CI(h,p) includes only a small portion of dynamic correlation.[32] This is expected to have an impact on transition-metal complexes, where a high level of correlation is needed for accurate description of relevant states.

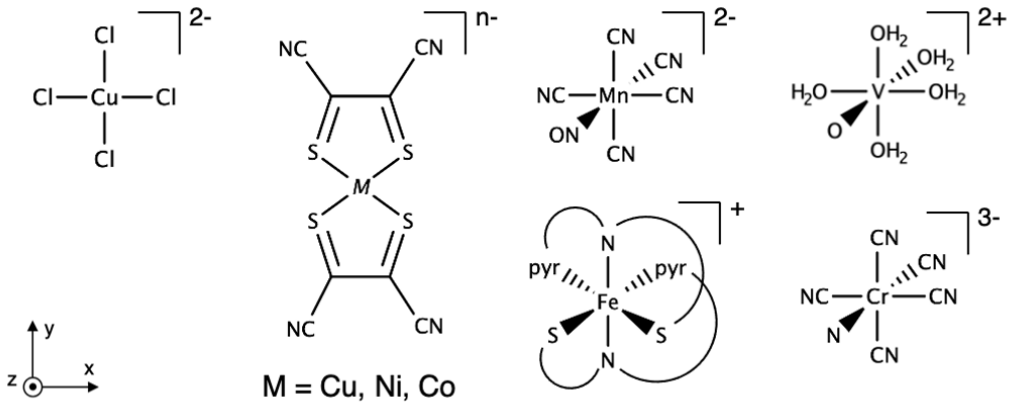

FIG. 4: Transition-metal complexes studied. N-2-mercapto-2-methyl-propyl-2'-pyridylmethyl eniminato (PyMS) ligand in $[Fe(PyMS)_2]^+$ is depicted in a simplified way.

A. Molecules composed of light atoms

Table I compares g-tensor shifts computed by the state-interaction approach using EOM-IP-CCSD, RAS-CI, and CASPT2 treatments with the CCSD response theory results and experimental data (CASPT2 results are from Ref. 39). The CCSD state used for the EOM-IP and response calculations is the lowest-energy solution corresponding to the closed-shell reference. The analysis uses Mulliken's molecular orientation.[57]

TABLE I: Ground-state Δg values for molecules composed of light elements computed with EOM-IP, RAS-CI, and CCSD (response) with the def2-TZVP basis set, and compared to CASPT2 and experimental values.

molecule		EOM-IP	RAS-CI	CCSD	CASPT2[a]	Exp.[a]
H_2O^+	Δg_{xx}	-0.1	0.0	0.1	–	0.2
	Δg_{yy}	16.0	15.2	15.4	15.6	18.8
	Δg_{zz}	4.8	4.0	4.5	3.9	4.8
NO_2	Δg_{xx}	3.8	2.5	3.8	3.8	3.9
	Δg_{yy}	-3.4	-9.5	-10.8	-12.1	-11.3
	Δg_{zz}	-0.3	-0.4	-0.5	1.5	-0.3
CO_2^-	Δg_{xx}	1.1	-0.3	1.3	1.0	0.7
	Δg_{yy}	-1.9	-4.1	-5.0	-5.8	-4.8
	Δg_{zz}	-0.9	-0.4	-0.6	–	-0.5

[a] CASPT2 and experimental results are from Ref. 39.

EOM-IP calculations based on the default Hartree–Fock reference show varying agreement with the experimental results. RAS-CI and CCSD (response) g-tensor shifts agree well

with the experiment for all three molecules. The CASPT2 results also match the experimental values well, except for the Δg_{zz} component of NO_2.

In H_2O^+, the spin-doublet ground state belongs to B_1 irreducible representation (irrep). Consistent with the symmetry selection rules, Δg_{xx}, Δg_{yy}, and Δg_{zz} result from interactions of the ground state with states of A_2, A_1, and B_2 irreps, respectively. All methods show the same deviation of 3 ppt in Δg_{yy} relative to the experimental value, consistent with the previous MRCI studies.[59, 60]

Table S2 in the SI illustrates the dependence of the Δg values on the number of states included in the state-interaction calculations for EOM-IP using water cation. For both EOM-IP and RAS-CI (not shown), the computed g-tensor shifts reach a qualitative agreement with the experimental values with just one state per irrep and change by less than 0.25 ppt upon including higher-energy states. Thus, for this molecule the state-interaction scheme converges quickly and smoothly with respect to the number of states included in the calculation. However, this is not the case for other examples (see, for example, Fig. S5 in the SI; more on this below).

In NO_2 and CO_2^-, the ground state is of A_1 symmetry and Δg_{xx}, Δg_{yy}, and Δg_{zz} arise from the interactions with B_2, B_1, and A_2 states, respectively. For NO_2, the EOM-IP value of the Δg_{yy} component of the g-tensor is less than half the experimental value. RAS-CI results show good qualitative agreement, but yield too-low absolute values for Δg_{xx} and Δg_{yy} due to the insufficient treatment of dynamic correlation.

For CO_2^-, RAS-CI underestimates Δg_{yy} and yields a wrong sign for Δg_{xx}. For EOM-EA calculation, only Δg_{zz} is in qualitative agreement with experiment, whereas the Δg_{xx} and Δg_{yy} components do not match the experimental values, and Δg_{xx} has a wrong sign. We attribute the disappointing performance of EOM-IP for NO_2 and EOM-EA for CO_2^- to the failure of the chosen combination of the EOM model and the reference configuration to describe all important state interactions on an equal footing and, therefore, cannot be remedied by increasing the number of states included in the calculation. This means that response-theory calculations using these methods (EOM-IP/EA) will suffer from the same problem. In the following, we provide a detailed analysis and ways to improve the results.

1. *The effect of the reference in EOM-IP/EA calculations: NO_2 and CO_2^- examples*

By analyzing the EOM-IP states that contribute to the SOC Hamiltonian, Eq. (6), the discrepancies relative to experiment can be explained and the results improved. As reported by Bolvin,[39] large contributions to the g-tensor arise when there is a large transition angular momentum between an excited state and the ground state. For the three molecules discussed here, this requirement is only fulfilled by excitations within the partially occupied frontier orbitals derived from the respective atomic p-orbitals, as expected from the El-Sayed's rules.[61, 62] Thus, for these molecules each g-tensor component is dominated by very few or even only one excited state.

In NO_2, the ground state (X^2A_1) is described by the electron configuration $[5114]6a_1^1$ (five doubly occupied orbitals of A_1, one of A_2, one of B_1, and four of B_2 symmetries, and one singly occupied $6a_1$ orbital). The Δg_{xx} component is dominated by the 2^2B_2 state with the $[6113]3b_2^1$ configuration. The Δg_{yy} component is dominated by the 1^2B_1 state with the $[5114]4b_1^1$ configuration. The Δg_{zz} component is dominated by the 7^2A_2 state with three unpaired electrons in the $[5113]6b_1^1 2b_1^1 4b_2^1$ configuration.

The data presented in Table I uses the reference state corresponding to the closed-shell configuration [6114]. As we identify the excitations necessary to obtain our target ground state and the respective dominant excited states for each Δg component, the picture becomes clearer. For the Δg_{xx} component, both the ground and dominant excited states are connected to the reference state via removal of an electron from a single orbital—the $6a_1$ orbital for the ground state and the $3b_2$ orbital for the dominant 2^2B_2 state. However, to reach the major contributing state to the Δg_{yy} component, i.e., the 1^2B_1 state, it is necessary to remove two electrons from the $6a_1$ orbital and add an electron to the $4b_1$ orbital. To connect the reference configuration to 7^2A_2 (responsible for the Δg_{zz} component), two electrons need to be removed—one from the $6a_1$ and one from the $2b_1$ orbitals—and one electron needs to be added to the $4b_2$ orbital.

Because the configurations generated from the reference state by higher excitation levels (e.g., $2h1p$ in EOM-IP) are described less accurately than configurations generated by lower-level excitations (e.g., $1h$), both the energy differences and transition properties involving these states are affected, which explains the errors in the Δg_{yy} and Δg_{zz} components. To illustrate how one can circumvent this problem, we recomputed the g-shift of NO_2 using other

reference states and in one case using EOM-EA instead of EOM-IP to ensure that the ground and dominant excited states are generated at the same excitation level. Specifically, we used EOM-EA based on a [5114] reference configuration to improve the Δg_{yy} component and EOM-IP based on a [5124] reference configuration to investigate the mismatch in excitation levels for the Δg_{zz} component.

TABLE II: Shifts in the g-matrix components (in ppt) of NO_2 molecule computed at the EOM-XX-CCSD/def-TZVP level with different reference configurations and excitation operators (XX = IP, EA).

	EOM-IP/[6114]	EOM-EA/[5114]	EOM-IP/[5124]	Exp.[a]
Δg_{xx}	3.8	1.6	-0.0	3.9
Δg_{yy}	-3.4	-11.2	-11.0	-11.3
Δg_{zz}	-0.3	0.8	-0.0	-0.3

From Ref. 39.

Table II presents the g-tensor shifts computed using these three different references ([6114], [5114], and [5124]). For each of the reference configuration, the g-matrix component for which the configuration was selected for agrees well with the experimental value. EOM-IP based on the reference with the [6114] configuration results in a good agreement between the computed Δg_{xx} and Δg_{zz} components and the experiment. EOM-EA based on the [5114] reference configuration results in a good agreement for the Δg_{yy} component and EOM-IP based on the [5124] reference configuration results in a good agreement for the Δg_{zz} component. Whereas the Δg_{zz} component computed with the [6114] reference is in better agreement with the experimental value than the one obtained from the [5124] reference that was specifically selected for its calculation, the difference between the results is within the range of deviations observed for other components.

TABLE III: Shifts in the g-matrix components (in ppt) of CO_2^- molecule computed at the EOM-XX-CCSD/def-TZVP level with different reference configurations and excitation operators (XX = IP, EA).

	EOM-EA/[5114]	EOM-IP/[6114]	Exp.[a]
Δg_{xx}	0.1	1.1	0.7
Δg_{yy}	-5.0	-1.9	-4.8
Δg_{zz}	-0.2	-0.9	-0.5

From Ref. 39.

In the same way, optimal reference configurations can be selected for each component of the g-tensor of CO_2^-, as illustrated in Table III. The ground state, X^2A_1, is dominated by

the configuration $[5114]6a_1^1$. EOM-IP based on the [6114] configuration describes well several states that make dominant contributions to the Δg_{xx} component as well as the $[6014]1a_2^1$ configuration that dominates the Δg_{zz} component. For the Δg_{zz} component, the dominant configuration is $[6104]b_1^1$, which is better described by EOM-EA based on the [5114] reference.

2. *Analysis of RAS-CI results*

To determine the main cause for the discrepancies of RAS-CI results with respect to experimental g-shifts, we first explore the impact of the errors in the excitation energies to the main contributing states. For that, we calculate Δg values by replacing the RAS-CI state energies with the experimental (when available) or accurate computational values in the relativistic Hamiltonian (Eq. (6)), while using RAS-CI interstate SOCs and angular momentum matrix elements. Table IV shows the results of these calculations.

TABLE IV: RAS-CI and best estimated excitation energies (ΔE in eV) to the states responsible for the dominant contributions to Δg_{kk} (ppt, $k = x, y, z$). RAS-CI(c) denotes Δg computed with the reference (best) energies.

		ΔE			Δg_{kk}		
molecule	sym.	RAS-CI	best	k	RAS-CI	RAS-CI(c)	best
H_2O^+	A_1	2.0	2.1[a]	y	15.2	15.1	18.8[a]
	B_2	6.6	5.9[a]	z	4.0	4.4	4.8[a]
NO_2	B_2	10.4	7.7[b]	x	2.5	3.3	3.8[a]
	B_1	3.0	2.8[a]	y	-9.5	-10.1	-11.7[a]
	A_2	12.6	9.8[a]	z	-0.4	-0.1	0.5[a]
CO_2^-	B_2	9.9	8.9[b]	x	-0.3	-0.2	1.0[b]
	B_1	3.7	3.4[b]	y	-4.1	-4.5	5.8[b]

[a] Using experimental energies from Ref. 60. [b] Using CASPT2 energies from Ref. 39.

In H_2O^+, RAS-CI excitation energy to 1^2A_1 is very close to the experimental value. Therefore, the corrected RAS-CI Δg_{yy} in H_2O^+ barely changes with respect to the original RAS-CI calculation. However, the RAS-CI energy for 1^2B_2 is 0.7 eV too high and using corrected energy indeed improves Δg_{zz}. Similarly, RAS-CI excitation energies for the states with dominant contributions to Δg components in NO_2 are overestimated. Correcting transition energies in H^{eff} noticeably improves g-tensor shifts. Finally, correction of excitation energies in CO_2^- improves Δg_{yy}, but has a rather small effect on Δg_{xx}, despite the fact that it involves a correction of 1 eV in the excitation energy of a high-lying B_2 state.

In summary, replacing excitation energies in H^{eff} (diagonal terms) with more accurate values is a simple and efficient strategy to improve Δg from RAS-CI. In the spirit of composite approaches, this provides a simple strategy to mitigate the consequences of the lack of dynamical correlation in RAS-CI in the computation of g-matrix elements. However, the missing electron correlation in RAS-CI might not only affect the accuracy of excitation energies, but also tune the character of electronic states thus affecting the computed spin–orbit and angular momentum interstate couplings. These effects cannot be recovered by the simple shift of excitation energies.

B. First-Row Transition-Metal Complexes

We now proceed to calculations of ground-state g-tensor shifts for the first-row transition-metal complexes featuring various electronic configurations and coordination patterns (Fig. 4). We anticipate strong dependence of g-tensors computed with single-reference EOM-CC and RAS-CI approaches on the chosen reference determinant. In general, reference configurations with empty (d^0), fully occupied (d^{10}), or semi-occupied (high-spin d^5) metal $3d$-shell are preferred due to symmetry (correct description of orbital degeneracies) and energy (better treatment of d-d energy gaps) considerations. For example, complexes with nine d-electrons, such as Cu(II) complexes, can be well described by removing an electron from a closed-shell d^{10} reference state, whereas complexes with one d-electron, such as Cr(V) compounds, can be well described by electron attachment to a d^0 reference configuration.

Below, we organize the discussion of the results based on the electronic configuration of the metal, i.e., d^9, d^7, d^5, and d^1 complexes. In all cases, we explore the performance of the state-interaction approach using EOM-CC/MP2 and RAS-CI treatments, and compare them with the CCSD response values, NEVPT2 results from Singh *et al.*[44], and with the experimental data.

1. d^9 complexes: $[CuCl_4]^{2-}$ and $[Cu(mnt)_2]^{2-}$

Table V shows g-tensor shifts for the two investigated d^9 complexes, $[CuCl_4]^{2-}$ and $[Cu(mnt)_2]^{2-}$. The g-tensor shifts computed with the EOM-IP, RAS-CI, and linear-response CCSD agree rather well with the previous calculations[44] using NEVPT2 and the experi-

mental values.[63, 64] In general, RAS-CI overestimates Δg (in all directions) with respect to experiment, similar to NEVPT2 calculations. The errors in the linear response CCSD shifts are considerably smaller, although they are still too large. In all cases, EOM-IP gives the best results.

TABLE V: Δg values (in ppt) for $[CuCl_4]^{2-}$ and $[Cu(mnt)_2]^{2-}$ complexes computed with the EOM-IP, RAS-CI (state-interaction), and CCSD (response) approaches and compared with the NEVPT2 and experimental values.

Complex		EOM-IP	RAS-CI	CCSD	NEVPT2[a]	Exp.[b]
$[CuCl_4]^{2-}$	Δg_{xx}	46	67	66	77	44
	Δg_{yy}	46	67	66	77	44
	Δg_{zz}	289	398	332	454	218
$[Cu(mnt)_2]^{2-}$	Δg_{xx}	25	69	32	56	21
	Δg_{yy}	25	72	34	57	24
	Δg_{zz}	116	329	140	238	84

[a] From Ref. 44. [b] Experimental values for $[CuCl_4]^{2-}$ and $[Cu(mnt)_2]^{2-}$ are from Refs. 63 and 64, respectively.

In order to rationalize the errors in our calculations, in particular the systematic overestimation of Δg by RAS-CI, we analyze the results for $[CuCl_4]^{2-}$. The ground state of $[CuCl_4]^{2-}$ has a square planar (D_{4h}) geometry. The electronic configuration is X^2B_{1g}, with the unpaired electron residing on the molecular orbital derived from the σ-antibonding combination of the $3d_{x^2-y^2}$ orbital of the metal and the symmetry-adapted combination of the (p_x, p_y)-orbitals of the ligands (Fig. 5).

Analysis of the dependence of Δg values on the number of excited states included in the Hamiltonian treated within the quasi-degenerate perturbation theory,[65] Eq. (6), indicates that the lowest excitations are the main contributions to the computed values (Fig. 5). Specifically, the first excited state (1^2B_{2g}), with the unpaired electron on the copper's d_{xy} orbital, results in the largest shift in g_{zz}, whereas the twofold degenerate 1^2E_g state, with the spin density mostly on the (d_{xz}, d_{yz}) orbital pair, is the main contributor to Δg_{xx} and Δg_{yy}. The positive sign of the computed shifts in the three directions can be rationalized by the nature of the electronic transitions from the ground state to 1^2B_{2g} and 1^2E_g, i.e., electron promotions from doubly occupied molecular orbitals to the ground-state singly occupied molecular orbital (SOMO), as expected from the ligand-field theory.[66]

By considering the perturbative SOC correction of the Kramers-pair wave function,[39] one can attribute the deviation of the RAS-CI Δg values to the errors in the interstate SOCs

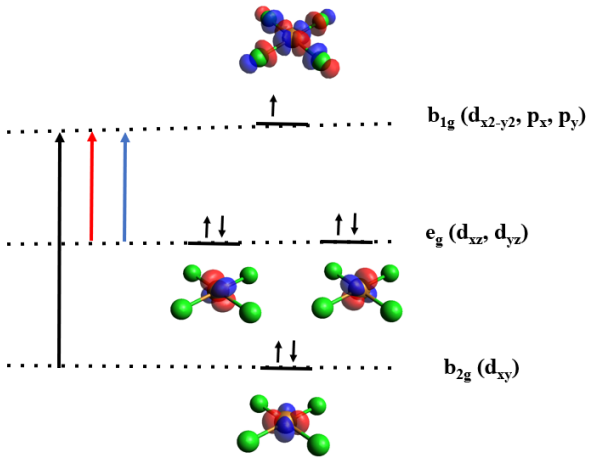

FIG. 5: Frontier molecular orbitals describing the main electronic transitions from the ground (X^2B_{1g}) to the excited 1^2B_{2g} and 1^2E_g states of $[CuCl_4]^{2-}$.

and energy gaps (Eq. 6 in Ref. 44). In particular, within the state-interaction approach, the change in the g-shifts induced by an excited state increases with the strength of the SOC and decreases with the increase of the energy gap. Therefore, the overestimation of SOCs and the underestimation of excitation energies result in too large Δg. In this case, both the errors in the transition energies and SOCs between the ground and the low-lying excited states of $[CuCl_4]^{2-}$ obtained at the RAS-CI level (Table VI) contribute to the overall overestimation of Δg values. Hence, we conclude that the missing electron correlation in the RAS-CI ansatz noticeably affects the accuracy of the energy gaps and the character of the electronic wave functions, e.g., spin density distribution, and that both effects result in too-large Δg values (Table S5 in the SI).

TABLE VI: Excitation energies (ΔE, in eV) and SOC constants (SOCC in cm^{-1}) between the ground state and 1^2B_{2g} and 1^2E_g excited states of $[CuCl_4]^{2-}$ described with the EOM-IP and RAS-CI.

	ΔE			SOCC	
State	RAS-CI	EOM-IP	Exp.[b]	RAS-CI	EOM-IP
1^2B_{2g}	1.315	1.446	1.552	1022	890
1^2E_g	1.604	1.725	1.763	498	412

From Ref. 63.

Coordination with the bidentate maleonitriledithiolate (mnt) ligand reduces the molecular symmetry of $[Cu(mnt)_2]^{2-}$ to D_{2h}, lifting the degeneracy between Δg_{xx} and Δg_{yy}. The ground-state spin density in this compound corresponds to a non-bonding d_{xy} orbital, giving

rise to the X^2B_{1g} state. The shifts in the g-tensor components arise, for the most part, from the interaction of the ground state with the lowest $^2B_{2g}$ (Δg_{xx}), $^2B_{3g}$ (Δg_{yy}), and ^2A_g (Δg_{zz}) excited doublets, respectively derived from the electronic transition between the doubly occupied d_{xy} orbital and the unoccupied d_{xz}, d_{yz}, and $d_{x^2-y^2}$ (Fig. S1 in the SI), respectively.

2. d^7 complexes: $[Co(mnt)_2]^{2-}$ and $[Ni(mnt)_2]^-$

The two studied d^7 complexes, $[Co(mnt)_2)]^{2-}$ and $[Ni(mnt)_2]^-$, have a D_{2h} ground-state structure, with an unpaired electron on the molecular orbital involving the d_{yz} orbital of the metal, giving rise to the X^2B_{3g} configuration. Symmetry selection rules applied to the perturbative expression of the ground-state Δg, Eq. (11), predict that excited states contributing to the shifts in the xx, yy, and zz directions should belong to the A_g, B_{1g}, and B_{2g} irreps, respectively. Table VII shows computed Δg for $[Co(mnt)_2)]^{2-}$ and $[Ni(mnt)_2]^-$. EOM-IP and RAS-CI g-tensor components for the $[Co(mnt)_2)]^{2-}$ complex are in qualitative agreement with the NEVPT2[44] and experimental values.[67] Interestingly, EOM-IP improves upon the NEVPT2 values, especially for the xx-component, which is overestimated by the latter by more than 400 ppt. On the other hand, RAS-CI underestimates the principal xx-component by 250 ppt and notably improves Δg_{yy} with respect to NEVPT2 and EOM-IP, while overestimating Δg_{zz}.

TABLE VII: Δg (in ppt) for $[Co(mnt)_2]^{2-}$ and $[Ni(mnt)_2]^-$ complexes computed at the EOM-MP2, RAS-CI (state-interaction) and CCSD (response with SVPD basis) levels, and compared to the NEVPT2 and experimental values.

Complex		EOM-MP2	RAS-CI	CCSD	NEVPT2[a]	Exp.
$[Co(mnt)_2]^{2-}$	Δg_{xx}	868	549		1207	796[b]
	Δg_{yy}	-99	-43		-101	-25[b,d]
	Δg_{zz}	17	33		29	23[b,d]
$[Ni(mnt)_2]^-$	Δg_{xx}	37	-1	114	485	158[b],125[c]
	Δg_{yy}	37	28	48	74	40[b], 19[c]
	Δg_{zz}	-2	-4	3	-11	-4[b], -17[c]

[a] From Ref. 44. [b] From Ref .68. [c] From Ref .69. [d] Ref. 68 indicates $\Delta g_{yy} = 23$ and $\Delta g_{zz} = -25$ ppt, but since our calculations systematically produce $\Delta g_{yy} < 0$ and $\Delta g_{zz} > 0$, we have reassigned the experimental values accordingly.

In the ground state of $[Co(mnt)_2)]^{2-}$, the unpaired electron occupies the d_{yz} orbital of the

metal, with no involvement of the ligand orbitals (Fig. 6). The main contribution to Δg_{xx} comes from the lowest ^2A_g state, corresponding to the electron transition from a doubly occupied orbital with strong d_{z^2} character to the ground-state SOMO (d_{yz}), and exhibiting a rather strong spin–orbit interaction with X^2B_{3g} (SOCC = 614 cm^{-1} at the RAS-CI level). The much smaller magnitude for the yy and zz shifts can be rationalized in terms of larger energy gaps and weaker SOCs of the main contributing states, $^2B_{1g}$ ($d^1_{yz} \rightarrow d^0_{xy}$) and $^2B_{2g}$ ($d^2_{xz} \rightarrow d^1_{yz}$), respectively.

The spin-doublet ground electronic state of $[Ni(mnt)_2]^-$ also belongs to the B_{3g} irrep, but the spin density on the metal is considerably smaller than in the Co complex (Fig. 6). EOM-IP and RAS-CI produce rather accurate Δg_{yy} and Δg_{zz} values for $[Ni(mnt)_2]^-$, better than the respective NEVPT2 and CCSD response values, but are not able to reproduce the large shift in g_{xx}. EOM-IP largely underestimates Δg_{xx} (by 120 ppt) whereas the RAS-CI shift is very small (and negative). Such disagreement originates in the strong stabilization (large negative energy) of the doubly occupied d_{z^2} orbital in the Hartree–Fock reference employed in both approaches (EOM-IP and RAS-CI). As a result, the energy of the ^2A_g ($d^2_{z^2} \rightarrow$ SOMO) excited state responsible for Δg_{xx} is probably overestimated by EOM-IP, producing too low shifts in g_{xx}. RAS-CI calculations with 20 states are not even able to recover the excitation from d_{z^2} to the ground state SOMO, which explains the nearly zero shift in the xx-component.

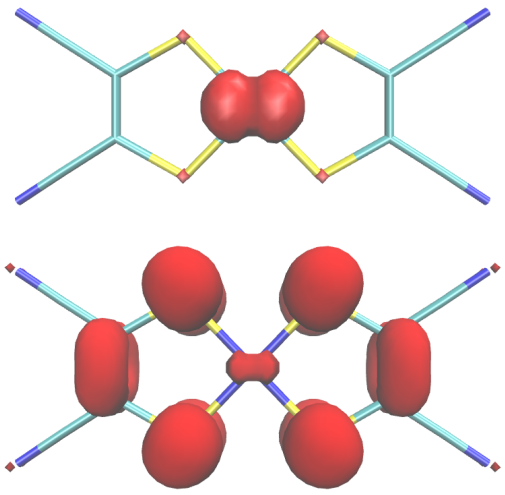

FIG. 6: Ground-state spin densities in $[Co(mnt)_2]^{2-}$ (top) and $[Ni(mnt)_2)]^-$ (bottom) computed at the RAS-CI/def3-TZVP level (iso value = 0.002).

3. d^5 complexes: $[Mn(CN)_5NO]^{2-}$ and $[Fe(PyMS)_2]^+$

Table VIII reports Δg values for the two investigated d^5 complexes, $[Mn(CN)_5NO]^{2-}$ and $[Fe(PyMS)_2]^+$. We note that Δg computed with EOM-MP2, RAS-CI, and CCSD (linear response) are in qualitative agreement with the experimental values, reproducing the correct order and signs of the shifts in the g-matrix components.

TABLE VIII: Δg shifts (in ppt) for $[Mn(CN)_5NO]^{2-}$ and $[Fe(PyMS)_2]^+$ complexes computed with EOM-MP2, RAS-CI (state-interaction), and CCSD (linear response), and compared to the NEVPT2 and experimental values. To achieve balanced description of the relevant states in EOM-MP2 calculations, Δg_{xx} and Δg_{yy} were computed by EOM-IP whereas Δg_{zz} was computed by EOM-EA.

complex		EOM-MP2	RAS-CI	CCSD	NEVPT2[b]	Exp.[c]
$[Mn(CN)_5NO]^{2-}$	Δg_{xx}	29	22[a]	9	17	24
	Δg_{yy}	29	22[a]	9	17	24
	Δg_{zz}	-34	-3	-11	0	-13
$[Fe(PyMS)_2]^+$	Δg_{xx}	59	27	78	106	88
	Δg_{yy}	41	13	34	-47	28
	Δg_{zz}	92	87	142	170	128

[a] Averaged xx and yy components ($\Delta g_{xx} = 28$ and $\Delta g_{yy} = 15$ ppt). [b] From Ref. 44. [c] From Refs. 70 and 71.

$[Mn(CN)_5NO]^{2-}$ has a C_{4v} symmetry and the X^2B_2 ground state, with the unpaired electron on the non-bonding d_{xy} orbital of the metal. The degenerate shifts of the g-components in the xy-plane result from the interaction of the ground state with the twofold ^2E excited state with a single unpaired electron in the π-bonding orbital between the (d_{xz}, d_{yz}) pair and the π-orbitals of the NO ligand (Fig. S3 in the SI). The main contribution to Δg_{zz} arises from the lowest $^2B_1$ state, derived by the electron transition from the doubly occupied π-bonding (d_{xz}, d_{yz}) orbitals to the π-antibonding (d_{xz}, d_{yz}) pair (Fig. S3 in the SI). EOM-IP and RAS-CI shifts in the xx and yy-directions agree well with the experiment, although RAS-CI artificially breaks the degeneracy between Δg_{xx} and Δg_{yy} as a consequence of the symmetry breaking in the ROHF reference (Fig. S5 in the SI). However, EOM-IP produces a too negative Δg_{zz} value whereas RAS-CI underestimates its magnitude. Linear-response CCSD and NEVPT2 underestimate Δg_{xx} and Δg_{yy}, and produce rather different results for the zz-component.

The $[Fe(PyMS)_2]^+$ complex (C_1 symmetry) has a doublet ground state with spin density on a non-bonding d_{z^2}-like orbital in the xy-plane (as shown in Fig. 4, the z-axis passes

through the metal and between the two S atoms). EOM-IP and RAS-CI recover qualitatively the experimental (positive) g-shifts, but systematically underestimate their magnitude, except for the yy-component with EOM-IP. CCSD response provides the most accurate Δg values, with errors within the 6-14 ppt range. Interestingly, we identified several low-lying states contributing to Δg_{zz} inducing either negative or positive shifts. Importantly, some sizeable $\Delta g_{zz} > 0$ contributions involve electron excitations from rather low-lying doubly occupied orbitals to the ground-state SOMO (Fig. S3 in the SI), which might explain the failure of NEVPT2 with a $(11, 13)$ active space[44] to recover the positive zz-shift.

4. d^1 complexes: $[VO(H_2O)_5]^{2+}$ and $[CrN(CN)_5]^{3-}$

$[CrN(CN)_5]^{3-}$ has a doublet ground state and C_{4v} geometry. This symmetry is also present in the first coordination shell of $[VO(H_2O)_5]^{2+}$ (VO_6 moiety), but it is lowered to C_2 when hydrogen atoms are included. Despite this symmetry lowering, we analyze both compounds in terms of the C_{4v} group, because hydrogen atoms have a minor effect on the frontier molecular orbitals in this molecule. Moreover, experiment indicates that, in solution, hydrogen atoms in $[VO(H_2O)_5]^{2+}$ appear as equivalent,[72, 73] probably due to dynamic averaging.

The ground state in both complexes (X^2B_2) has a single electron in the non-bonding d_{xy} orbital. The computed Δg components result from the interaction of X^2B_2 with excitations from the singly occupied d_{xy} to unoccupied orbitals with d character, consistent with the negative shifts in all directions (Table IX). Δg values in the xy-plane arise due to the interaction of the ground state with the lowest ^2E state, which has a single electron in the σ-antibonding orbital between the (d_{xz}, d_{yz}) of the metal and (p_x, p_y) of the ligands (Fig. 7). Δg_{zz} is dominated by the interaction with the lowest $^2B_1$ state with a spin density localized on the $d_{x^2-y^2}$ metal orbital (Fig. 7). All computational methods agree well with the experimental values. They correctly reproduce signs and ordering of the shifts, and yield absolute values that are close to the experimental values. In $[VO(H_2O)_5]^{2+}$, all methods yield accurate results. Only the magnitude of the zz-component obtained with RAS-CI is a bit too small, whereas EOM-MP2 and NEVPT2 underestimate the magnitude of Δg_{xx} and Δg_{yy}. In $[CrN(CN)_5]^{3-}$, EOM-MP2 and CCSD shifts are very close to experiment, with errors in the order of 2-4 ppt whereas RAS-CI yields too large $|\Delta g|$ values.

TABLE IX: Δg (in ppt) for the $[VO(H_2O)_5]^{2+}$ and $[CrN(CN)_5]^{3-}$ complexes computed with EOM-MP2, RAS-CI (state-interaction), and CCSD (response), and compared to the NEVPT2 and experimental values.

complex		EOM-MP2	RAS-CI	CCSD	NEVPT2[a]	Exp.
$[VO(H_2O)_5]^{2+}$	Δg_{xx}	-14	-18	-20	-14	-19[b]
	Δg_{yy}	-11	-18	-20	-14	-19[b]
	Δg_{zz}	-72	-58	-76	-78	-72[b]
$[CrN(CN)_5]^{3-}$	Δg_{xx}	-6	-10	-6	-4	-3[c]
	Δg_{yy}	-6	-10	-6	-4	-3[c]
	Δg_{zz}	-31	-43	-29	-42	-27[c]

[a] From Ref. 44. [b] From Ref. 72. [c] From Ref. 74.

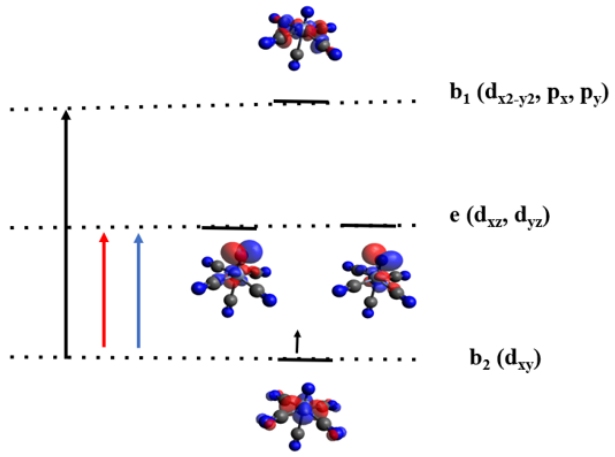

FIG. 7: Frontier molecular orbital diagram of $[CrN(CN)_5]^{3-}$ computed at the ROHF/def2-TZVP level.

5. *Non-innocent ligands and spin density distribution*

An accurate description of g-tensors requires a correct description of the metal-ligand bonding. The quality of the description is related to the spin density produced by different methods, which requires a proper correlation treatment of the metal-ligand interaction. Table X shows the spin density populations obtained with UHF, RAS-CI, and EOM-MP2 as well as the available experimental values.

Particularly interesting are the three dithiolate complexes. The non-innocent nature of the dithiolene ligand, manifested by the contribution of the ligand to the redox state of the transition metal ion,[75] strongly depends on the nature of the transition metal. For all the electronic structure methods, the magnitude of the computed spin density at the metal follows the $[Co(mnt)_2]^{2-} > [Cu(mnt)_2]^{2-} > [Ni(mnt)_2]^{-}$ order.

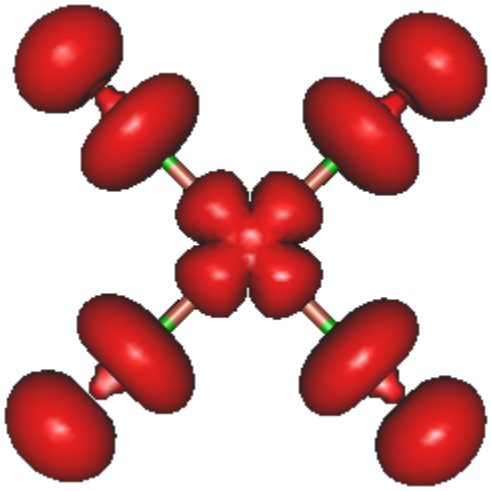

FIG. 8: Löwdin spin density of $[CuCl_4]^{2-}$ ground state computed at the EOM-IP-CCSD/def2-TZVP level.

TABLE X: Spin population of the metals in the ground state of transition-metal complexes computed with different electronic-structure methods.

complex	UHF	RAS-CI[a]	EOM-IP-MP2[b]	Exp.
$[CuCl_4]^{2-}$	0.87	0.75	0.64	0.62[c]
$[Cu(mnt)_2]^{2-}$	0.78	0.80	0.48	0.39[d]
$[Ni(mnt)_2]^{-}$	-0.07	0.01	0.20	0.32[d]
$[Co(mnt)_2]^{2-}$	1.04	0.93	0.76	-

[a] Mulliken analysis. [b] Löwdin analysis. [c] Obtained from adjusted Xα method.[76] [d] Derived from a combination of XAS and ENDOR spectroscopy.[77]

The mean-field (UHF) solution to the ground state overestimates the metal spin density in $[CuCl_4]^{2-}$ and $[Cu(mnt)_2]^{2-}$ compounds, but underestimates it in the nickel complex. Overall, electron correlation effects through the post-HF treatment in EOM-MP2 recover the experimental values, whereas the RAS-CI spin density on the metal shows only partial improvement upon UHF, especially in $[Ni(mnt)_2]^{-}$ for which the spin density on the Ni atom is very small.

A possible way to improve this result is by changing the Hartree–Fock reference to the Kohn–Sham DFT reference, which tends to yield more accurate ground state-spin densities.[78] Indeed, the ground-state spin population on the Ni using DFT orbitals increases to 0.46. Thus, using KS-DFT orbitals in RAS-CI calculations might help to obtain more accurate g-tensor values, similar to other uses of DFT orbitals in correlated calculations

of open-shell species.[33]

EOM-IP-MP2 and EOM-IP-CCSD provide rather accurate spin densities because of the effective inclusion of all configurations with single and double holes on the metal and on the ligand orbitals. As a result, for these complexes they produce the best g-tensor shifts (as compared to the experimental values, except for $[\mathrm{Ni(mnt)_2}]^-$) and also reproduces the trends in spin densities.

6. Comparison with NEVPT2 results

For the transition-metal complexes discussed by Neese and coworkers,[44] the performance of the state-interaction approach using EOM states depends on the number of d-electrons. Unsurprisingly, for d^9 EOM-IP and for d^1 EOM-EA perform well, nearly always better than active-space methods, especially, when the latter do not include the doubly occupied metal and ligand orbitals in the active space. For d^7, EOM-IP results are of mixed quality—worse than NEVPT2 for the Co complex and better than NEVPT2 for the Ni complex (although still not great). It would be interesting to see how other EOM methods (e.g., double EA or triple IP) perform for these systems, once the requisite properties are implemented.

C. Solvent Effects

We use $[\mathrm{Co(mnt)_2}]^{2-}$ complex to investigate effects of the solvent on g-tensors. Neese and co-workers[44] reported that solvent effects are relatively modest, e.g., contributing less than 10 percent change in Δg. For the $[\mathrm{Co(mnt)_2}]^{2-}$ complex, our EOM-IP results in an xx-component of 868 ppt with CPCM and 1172 without which is an significant improvement towards the experimental value of 795 ppt, as shown in Table XI.

The large differences in Δg computed with and without solvent are caused mostly by the change in energy gaps, i.e., 0.007 versus 0.01 eV for the def2-TZVP results. However, the solvent also affects spin densities. Fig. 9 illustrates the effect of the solvent on the singly occupied natural orbital in the $\mathrm{Co(mnt)_2^{2-}}$ complex. The isosurfaces containing 99.5 % of electron density without solvent effect and including CPCM reveal that the singly occupied natural orbital is localized on the Co center when no solvent effects are included, as it has been shown in Fig. 6. When CPCM is added, the orbital is distributed more evenly over the

TABLE XI: Solvent effect on the computed EOM-IP-MP2 Δg (in ppt) for $[Co(mnt)_2]^{2-}$ complex.

	Δg_{xx}	Δg_{yy}	Δg_{zz}
$[Co(mnt)_2]^{2-}$			
exp.	796	-25	23
def2-TZVP, symmetry, no solvent	1172	-187	-85
def2-TZVP, no symmetry, CPCM	868	-99	17
def2-SVPD, symmetry, no solvent	1746	-323	-439
def2-SVPD, no symmetry, no solvent	1736	-319	-433
def2-SVPD, no symmetry, CPCM	1321	-99	-237
$[Ni(mnt)_2]^{-}$			
exp.	39	157	-4.3
def2-TZVP, symmetry, no solvent	37	37	-2
def2-TZVP, no symmetry, CPCM	32	33	-1

sulfur atoms of the ligands—this can be explained in terms of solvent screening electrostatic interactions and therefore stabilizing charge-transfer character, which moves the spin density away from the metal thus reducing the SOCC.

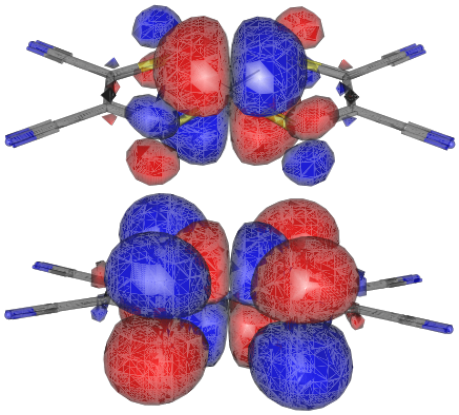

FIG. 9: Singly occupied natural orbital in $Co(mnt)_2^{2-}$ without including solvent effects (top) and including solvent effects via CPCM (bottom).

IV. CONCLUSIONS

We presented a protocol for computing g-tensors using state-interaction framework, following the work of Bolvin.[39] The main advantage of this approach relative to response theory is that it can be applied with relative ease to any quantum chemistry method that can furnish spin–orbit couplings and matrix elements of the angular momentum operators. Moreover, within this protocol, different electronic structure models can be combined in the spirit of composite approaches or externally corrected methods. The disadvantage is that the protocol is not black-box and careful analysis of the convergence with respect to the zero-order states is required.

We applied this protocol to the EOM-CC and RAS-CI methods using a set of open-shell molecules, including transition-metal complexes. We only investigated doublet states, but the approach can be extended to other multiplicities. The results show that both treatments can deliver accurate results within this framework. For comparison, we also presented results obtained with CCSD response-theory approach. In addition to the g-tensor values, we also discussed the underlying spin densities. We carefully analyzed the results in terms of underlying molecular orbitals and wave function to explain the relative importance of leading contributions; this analysis provides insight into the strengths and weaknesses of the quantum-chemistry methods employed.

In our analysis, we highlighted the issues faced by EOM-CC and RAS-CI. Both methods are sensitive to the reference choice, and, as in other properties calculation, the quality of the computed property depends not only by the quality of the state itself, but also on the quality of excited states —or, more generally, spectral properties of the model Hamiltonian. Importantly, this issue—sensitivity to the spectral properties—will, most likely, affect the quality of the results within response-theory implementation, in a similar fashion as was observed in calculations of non-linear optical properties using the EOM-CC framework.[79, 80] Our analysis of difficult cases (such as NO_2) can provide insights into the performance of other methods in the context of g-tensors calculations.

RAS-CI method affords greater flexibility than EOM-IP by virtue of producing more excited states by careful selection of the active space, but the results may be affected by the insufficient treatment of dynamic correlation and the sensitivity to the reference orbitals.

We also discussed other factors affecting g-tensors, such as basis sets and solvent effects.

In conclusion, our work introduces a useful tool for computational studies of magnetic molecules, including transition-metal complexes, and also contributes towards a better understanding of the effects of correlation treatment on magnetic properties.

Supporting information

Description of the *Python* post-processing script; inputs for EOM-CC and RAS-CI calculations; Cartesian geometries; active-space selection; convergence analysis.

Acknowledgments

S.K. and A.C. contributed equally.

We thank Prof. Jürgen Gauss from the Johannes Gutenberg University in Mainz for his help and guidance in the implementation of the CCSD response calculations of g-tensors.

The work in Los Angeles was supported by the National Science Foundation through the "CCI Phase I: NSF Center for Advanced Molecular Architectures for Quantum Information Science" grant (Award CHE-2221453).

S.K. acknowledges support by Walter-Benjamin fellowship from the German Research Foundation (DFG) (project 441274206).

The work at the DIPC was funded by the Spanish Government MICINN (projects PID2019-109555GB-I00, PID2022-136231NB-I00 and PRE2020-094317), the Gipuzkoa Provincial Council (project QUAN-000021-01), the European Union (project NextGenerationEU/PRTR-C17.I1), as well as by the IKUR Strategy under the collaboration agreement between Ikerbasque Foundation and DIPC on behalf of the Department of Education of the Basque Government. The authors are thankful for the technical and human support provided by the Donostia International Physics Center (DIPC) Computer Center. D.C. is thankful for financial support from IKERBASQUE (Basque Foundation for Science).

The authors declare the following competing financial interest(s): A.I.K. is the president and a part-owner of Q-Chem, Inc.

References

[1] Zavoisky, E. Spin-magnetic resonance in paramagnetics *J. Phys. USSR* **1945**, *9*, 211–245.

[2] Harriman, J. E. *Theoretical foundations of electron spin resonance;* Academic Press: New York, 1978.

[3] Neese, F. In *High Resolution EPR: Applications to Metalloenzymes and Metals in Medicine*; Berliner, L., Hanson, G., Eds.; Springer New York: New York, NY, 2009; p. 175.

[4] Holm, R. H.; Kennepohl, P.; Solomon, E. I. Structural and functional aspects of metal sites in biology *Chem. Rev.* **1996**, *96*, 2239–2314.

[5] Takahashi, S.; Tupitsyn, I. S.; van Tol, J.; Beedle, C. C.; Hendrickson, D. N.; Stamp, P. C. E. Decoherence in crystals of quantum molecular magnets *Nature* **2011**, *476*, 76–79.

[6] Atanasov, M.; Aravena, D.; Suturina, E.; Bill, E.; Maganas, D.; Neese, F. First prinicples approach to the electronic structure, magnetic anisotropy and spin relaxation in mononuclear 3d-transition metal single molecular magnets *Coord. Chem. Rev.* **2015**, *289-290*, 177–214.

[7] Neese, F. Quantum chemical calculations of spectroscopic properties of metalloproteins and model compounds: EPR and Mössbauer properties *Curr. Opin. Chem. Biol.* **2003**, *7*, 125–135.

[8] Dikanov, S. A.; Crofts, A. R. In *Handbook of Applied Solid State Spectroscopy*; Vij, D. R., Ed.; Springer US, 2006; p. 97.

[9] Roessler, M. M.; Salvadori, E. Principles and applications of EPR spectroscopy in the chemical sciences *Chem. Soc. Rev.* **2018**, *47*, 2534–2553.

[10] van der Est, A. In *eMagRes;* John Wiley & Sons, 2016; p. 1411.

[11] de Graaf, C.; Broer, R. *Magnetic interactions in molecules and solids;* Springer Cham, 2016.

[12] Perera, A.; Gauss, J.; Verma, P.; Morales, J. A. Benchmark coupled-cluster g-tensor calculations with full inclusion of the two-particle spin-orbit contributions *J. Chem. Phys.* **2017**, *146*, 164104.

[13] Linderberg, J.; Öhrn, Y. *Propagators in quantum chemistry;* Academic, London, 1973.

[14] Helgaker, T.; Coriani, S.; Jørgensen, P.; Kristensen, K.; Olsen, J.; Ruud, K. Recent advances in wave function-based methods of molecular-property calculations *Chem. Rev.* **2012**, *112*, 543–631.

[15] Gerloch, M.; McMeeking, R. F. Paramagnetic properties of unsymmetrical transition-metal

complexes *J. Chem. Soc., Dalton Trans.* pages, 2443–2451.

[16] Lushington, G. H.; Bündgen, P.; Grein, F. Ab initio study of molecular g-tensors: MOLECULAR g-TENSORS *Int. J. Quant. Chem.* **1995**, *55*, 377–392.

[17] Lushington, G. H.; Grein, F. Complete to second-orderab initio level calculations of electronicg-tensors *Theor. Chim. Acta* **1996**, *93*, 259–267.

[18] Lushington, G. H.; Grein, F. The electronicg-tensor of MgF: A comparison of ROHF and MRD-CI level results *Int. J. Quant. Chem.* **1996**, *60*, 1679–1684.

[19] Engström, M.; Vahtras, O.; Ågren, H. Hartree-Fock linear response calculations of g-tensors of substituted benzene radicals *Chem. Phys.* **1999**, *243*, 263–271.

[20] Schreckenbach, G.; Ziegler, T. Calculation of the g-tensor of electron paramagnetic resonance spectroscopy using gauge-including atomic orbitals and density functional theory *J. Phys. Chem. A* **1997**, *101*, 3388–3399.

[21] van Lenthe, E.; Wormer, P. E. S.; van der Avoird, A. Density functional calculations of molecular g-tensors in the zero-order regular approximation for relativistic effects *J. Chem. Phys.* **1997**, *107*, 2488–2498.

[22] Malkina, O. L.; Vaara, J.; Schimmelpfennig, B.; Munzarová, M.; Malkin, V. G.; Kaupp, M. Density functional calculations of electronic g-tensors using spin–orbit pseudopotentials and mean-field all-electron spin–orbit operators *J. Am. Chem. Soc.* **2000**, *122*, 9206–9218.

[23] Vahtras, O.; Minaev, B.; Ågren, H. Ab initio calculations of electronic g-factors by means of multiconfiguration response theory *Chem. Phys. Lett.* **1997**, *281*, 186–192.

[24] Gauss, J.; Kallay, M.; Neese, F. Calculation of electronic g-tensors using coupled cluster theory *J. Phys. Chem. A* **2009**, *113*, 11541–11549.

[25] Neese, F. Analytic derivative calculation of electronic g-tensors based on multireference configuration interaction wavefunctions *Mol. Phys.* **2007**, *105*, 2507–2514.

[26] Krylov, A. I. Equation-of-motion coupled-cluster methods for open-shell and electronically excited species: The hitchhiker's guide to Fock space *Annu. Rev. Phys. Chem.* **2008**, *59*, 433–462.

[27] Sneskov, K.; Christiansen, O. Excited state coupled cluster methods *WIREs: Comput. Mol. Sci.* **2012**, *2*, 566–584.

[28] Bartlett, R. J. Coupled-cluster theory and its equation-of-motion extensions *WIREs: Comput. Mol. Sci.* **2012**, *2*, 126–138.

[29] Mertins, F.; Schirmer, J. Algebraic propagator approaches and intermediate-state representations. I. The biorthogonal and unitary coupled-cluster methods *Phys. Rev. A* **1996**, *53*, 2140–2152.

[30] Dreuw, A.; Wormit, M. The algebraic diagrammatic construction scheme for the polarization propagator for the calculation of excited states *WIREs: Comput. Mol. Sci.* **2015**, *5*, 82–95.

[31] Casanova, D.; Head-Gordon, M. Restricted active space spin-flip configuration interaction approach: Theory, implementation and examples *Phys. Chem. Chem. Phys.* **2009**, *11*, 9779–9790.

[32] Casanova, D. Restricted active space configuration interaction methods for strong correlation: Recent developments *WIREs: Comput. Mol. Sci.* **2022**, *12*, e1561.

[33] Krylov, A. I. In *Reviews in Comp. Chem.*; Parrill, A. L., Lipkowitz, K. B., Eds., Vol. 30; J. Wiley & Sons, 2017; p. 151.

[34] Aoto, Y. A.; De Lima Batista, A. P.; Köhn, A.; De Oliveira-Filho, A. G. S. How to arrive at accurate benchmark values for transition metal compounds: Computation or experiment? *J. Chem. Theory Comput.* **2017**, *13*, 5291–5316.

[35] Malrieu, J. P.; Caballol, R.; Calzado, C. J.; de Graaf, C.; Guihéry, N. Magnetic interactions in molecules and highly correlated materials: Physical content, analytical derivation, and rigorous extraction of magnetic Hamiltonians *Chem. Rev.* **2013**, *114*, 429–492.

[36] Furlani, T. R.; King, H. F. Theory of spin-orbit coupling. Application to singlet-triplet interaction in the trimethylene biradical *J. Chem. Phys.* **1985**, *82*, 5577–5583.

[37] Berning, A.; Schweizer, M.; Werner, H.-J.; Knowles, P.; Palmieri, P. Spin-orbit matrix elements for internally contracted multireference configuration interaction wavefunctions *Mol. Phys.* **2000**, *98*, 1823–1833.

[38] Christiansen, O.; Gauss, J.; Schimmelpfennig, B. Spin-orbit coupling constants from coupled-cluster response theory *Phys. Chem. Chem. Phys.* **2000**, *2*, 965–971.

[39] Bolvin, H. An alternative approach to the g-matrix: Theory and applications *ChemPhysChem* **2006**, *7*, 1575–1589.

[40] Klein, K.; Gauss, J. Perturbative calculation of spin-orbit splittings using the equation-of-motion ionization-potential coupled-cluster ansatz *J. Chem. Phys.* **2008**, *129*, 194106.

[41] Epifanovsky, E.; Klein, K.; Stopkowicz, S.; Gauss, J.; Krylov, A. I. Spin-orbit couplings within the equation-of-motion coupled-cluster framework: Theory, implementation, and benchmark

calculations *J. Chem. Phys.* **2015**, *143*, 064102.

[42] Atanasov, M.; Ganyushin, D.; Pantazis, D. A.; Sivalingam, K.; Neese, F. Detailed ab initio first-principles study of the magnetic anisotropy in a family of trigonal pyramidal iron(II) pyrrolide complexes *Inorg. Chem.* **2011**, *50*, 7460–7477.

[43] Marian, C. M. Spin-orbit coupling and intersystem crossing in molecules *WIREs Comput. Mol. Sci.* **2012**, *2*, 187–203.

[44] Singh, S. K.; Atanasov, M.; Neese, F. Challenges in multireference perturbation theory for the calculations of the g-tensor of first-row transition-metal complexes *J. Chem. Theory Comput.* **2018**, *14*, 4662–4677.

[45] Pokhilko, P.; Epifanovsky, E.; Krylov, A. I. General framework for calculating spin–orbit couplings using spinless one-particle density matrices: theory and application to the equation-of-motion coupled-cluster wave functions *J. Chem. Phys.* **2019**, *151*, 034106.

[46] Vidal, M. L.; Pokhilko, P.; Krylov, A. I.; Coriani, S. Equation-of-motion coupled-cluster theory to model L-edge x-ray absorption and photoelectron spectra *J. Phys. Chem. Lett.* **2020**, *11*, 8314–8321.

[47] Carreras, A.; Jiang, H.; Pokhilko, P.; Krylov, A. I.; Zimmerman, P. M.; Casanova, D. Calculation of spin-orbit couplings using RASCI spinless one-particle density matrices: Theory and applications *J. Chem. Phys.* **2020**, *153*, 214107.

[48] Kotaru, S.; Pokhilko, P.; Krylov, A. I. Spinorbit couplings within spin-conserving and spin-flipping time-dependent density functional theory: Implementation and benchmark calculations *J. Chem. Phys.* **2022**, *157*, 224110.

[49] Roemelt, M. Spin orbit coupling for molecular ab initio density matrix renormalization group calculations: Application to g-tensors *J. Chem. Phys.* **2015**, *143*, 044112.

[50] Alessio, M.; Krylov, A. I. Equation-of-motion coupled-cluster protocol for calculating magnetic properties: Theory and applications to single-molecule magnets *J. Chem. Theory Comput.* **2021**, *17*, 4225–4241.

[51] Abragam, A.; Bleaney, B. *Electron paramagnetic resonance of transition ions;* Clarendon Press - Oxford, 1970.

[52] ezMagnet. Alessio, M.; Käler, S.; Cebreiro-Gallardo, A.; Pokhilko, P.; Kotaru, S.; Casanova, D.; Krylov, A. I.;
http://iopenshell.usc.edu/downloads/; accessed 08/20/2023.

[53] Casanova, D.; Krylov, A. I. Spin-flip methods in quantum chemistry *Phys. Chem. Chem. Phys.* **2020**, *22*, 4326–4342.

[54] Simons, J. In *Encyclopedia of computational chemistry;* J. Wiley & Son, New York, 1998.

[55] Epifanovsky, E.; Gilbert, A. T. B.; Feng, X.; Lee, J.; Mao, Y.; Mardirossian, N.; Pokhilko, P.; White, A. F.; Coons, M. P.; Dempwolff, A. L.; *et. al* Software for the frontiers of quantum chemistry: An overview of developments in the Q-Chem 5 package *J. Chem. Phys.* **2021**, *155*, 084801.

[56] Krylov, A. I.; Gill, P. M. W. Q-Chem: An engine for innovation *WIREs: Comput. Mol. Sci.* **2013**, *3*, 317–326.

[57] Mulliken, R. S. Report on notation for the spectra of polyatomic molecules *J. Chem. Phys.* **1955**, *23*, 1997–2011.

[58] Depending on molecular orientation, symmetry labels corresponding to the same orbital or vibrational mode may be different. Q-Chem's standard molecular orientation is different from that of Mulliken[57]. For example, Q-Chem would place water molecule in the xz plane instead of the yz. Consequently, for C_{2v} symmetry, b_1 and b_2 labels are flipped. More details can be found at http://iopenshell.usc.edu/resources/howto/symmetry/.

[59] Brownridge, S.; Grein, F.; Tatchen, J.; Kleinschmidt, M.; Marian, C. M. Efficient calculation of electron paramagnetic resonance g-tensors by multireference configuration interaction sum-over-state expansions, using the atomic mean-field spinorbit method *J. Chem. Phys.* **2003**, *118*, 9552–9562.

[60] Lushington, G. H.; Grein, F. Multireference configuration interaction calculations of electronic g-tensors for NO_2, H_2O^+, and CO^+ *J. Chem. Phys.* **1997**, *106*, 3292–3300.

[61] El-Sayed, M. A. Triplet state: Its radiative and non-radiative properties *Acc. Chem. Res.* **1968**, *1*, 8–16.

[62] Pokhilko, P.; Krylov, A. I. Quantitative El-Sayed rules for many-body wavefunctions from spinless transition density matrices *J. Phys. Chem. Lett.* **2019**, *10*, 4857–4862.

[63] Dick, A.; Rahemi, H.; Krausz, E. R.; Hanson, G. R.; Riley, M. J. The highly resolved electronic spectrum of the square planar $CuCl_4^{2-}$ ion *J. Chem. Phys.* **2008**, *129*, 214505.

[64] Kirmse, R.; Stach, J.; Dietzsch, W.; Hoyer, E. ^{33}S hyperfine interactions in the single-crystal ESR spectra of $(n\text{-}Bu_4N)^2$ $[^{63}Cu(mnt)_2]$ *Inorg. Chim. Acta* **1978**, *26*, L53–L55.

[65] Ganyushin, D.; Neese, F. First-principles calculations of zero-field splitting parameters *J.*

Chem. Phys. **2006**, *125*, 024103.

[66] Neese, F.; Solomon, E. I. Calculation of zero-field splittings, g-values, and the relativistic nephelauxetic effect in transition metal complexes. Application to high-spin ferric complexes *Inorg. Chem.* **1998**, *37*, 6568–6582.

[67] Gregson, A.K.; Martin, R.L.; Mitra, S. Paramagnetic anisotropy, ESR and electronic structure of square planar bis(dithioacetylacetonato)cobalt(II) *Chem. Phys. Lett.* **1970**, *5*, 310–311.

[68] Maki, A. H.; Edelstein, N.; Davison, A.; Holm, R. H. Electron paramagnetic resonance studies of the electronic structures of bis (maleonitriledithiolato) copper (II),-nickel (III),-cobalt (II), and-rhodium (II) complexes *J. Am. Chem. Soc.* **1964**, *86*, 4580–4587.

[69] Swartz, J. C.; Hoffman, B. M.; Krizek, R. J.; Atmatzidis, D. K. A general procedure for simulating EPR spectra of partially oriented paramagnetic centers *J. Mag. Res. (1969)* **1979**, *36*, 259–268.

[70] Fortman, J. J.; Hayes, R. G. Electron paramagnetic resonance studies of $Mn(CN)_5NO^{2-}$ and $Cr(CN)_5NO^{3-}$ in dilute single crystals *J. Chem. Phys.* **1965**, *43*, 15–22.

[71] Noveron, J. C.; Herradora, R.; Olmstead, M. M.; Mascharak, P. K. Low-spin iron (III) complexes with N, S coordination: syntheses, structures, and properties of bis (N-2-mercaptophenyl-2'-pyridylmethyleniminato) iron (III) tetraphenylborate and bis (N-2-mercapto-2-methylpropyl-2'-pyridylmethyleniminato) iron (III) tetraphenylborate *Inorg. Chim. Acta* **1999**, *285*, 269–276.

[72] Ballhausen, C. J.; Gray, H. B. The electronic structure of the vanadyl ion *Inorg. Chem.* **1962**, *1*, 111–122.

[73] Albanese, N. F.; Chasteen, N. D. Origin of the electron paramagnetic resonance line widths in frozen solution of the oxovanadium(IV) ion *J. Phys. Chem.* **1978**, *82*, 910–914.

[74] Bendix, J.; Deeth, R. J.; Weyhermüller, T.; Bill, E.; Wieghardt, K. Molecular and electronic structure of nitridocyanometalates of chromium (V) and manganese (V): A combined experimental and DFT study *Inorg. Chem.* **2000**, *39*, 930–938.

[75] Ray, K.; Petrenko, T.; Wieghardt, K.; Neese, F. Joint spectroscopic and theoretical investigations of transition metal complexes involving non-innocent ligands *Dalton Trans.* pages, 1552–1566.

[76] Szilagyi, R. K.; Metz, M.; Solomon, E. I. Spectroscopic calibration of modern density functional methods using $[CuCl_4]^{2-}$ *J. Phys. Chem. A* **2002**, *106*, 2994–3007.

[77] Sarangi, R.; DeBeer, G. S.; Rudd, D. J.; Szilagyi, R. K.; Ribas, X.; Rovira, C.; Almeida, M.; Hodgson, K. O.; Hedman, B.; Solomon, E. I. Sulfur K-edge x-ray absorption spectroscopy as a probe of ligand-metal bond covalency: Metal vs ligand oxidation in copper and nickel dithiolene complexes *J. Am. Chem. Soc.* **2007**, *129*, 2316–2326.

[78] Cramer, C. J.; Truhlar, D. G. Density functional theory for transition metals and transition metal chemistry *Phys. Chem. Chem. Phys.* **2009**, *11*, 10757–10816.

[79] Andersen, J. H.; Nanda, K. D.; Krylov, A. I.; Coriani, S. Cherry-picking resolvents: Recovering the valence contribution in x-ray two-photon absorption within the core-valence-separated equation-of-motion coupled-cluster response theory *J. Chem. Theory Comput.* **2022**, *18*, 6189–6202.

[80] Nanda, K.D.; Gulania, S.; ; Krylov, A. I. Theory, implementation, and disappointing results for two-photon absorption cross sections within the doubly electron-attached equation-of-motion coupled-cluster framework *J. Chem. Phys.* **2023**, *158*, 054102.

TOC Graphic

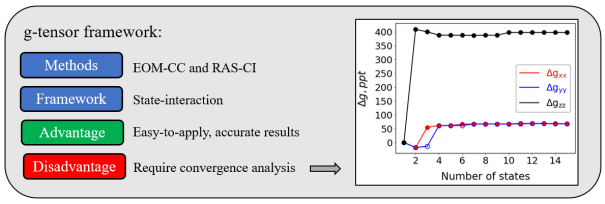
g-tensor framework:
Methods
EOM-CC and RAS-CI
Framework
State-interaction
Advantage
Easy-to-apply, accurate results
Disadvantage
Require convergence analysis
Δg, ppt
Number of states
Δgxx
Δgyy
Δgzz